Magnetic Resonance in Medicine 64:447–456 (2010)

O-Space Imaging: Highly Efficient Parallel Imaging Using Second-Order Nonlinear Fields as Encoding Gradients With No Phase Encoding

Jason P. Stockmann,[1]* Pelin Aksit Ciris,[1] Gigi Galiana,[2] Leo Tam,[1] and R. Todd Constable[3]

Recent improvements in parallel imaging have been driven by the use of greater numbers of independent surface coils placed so as to minimize aliasing along the phase-encode direction(s). However, gains from increasing the number of coils diminish as coil coupling problems begin to dominate and the ratio of acceleration gain to expense for multiple receiver chains becomes prohibitive. In this work, we redesign the spatial-encoding strategy in order to gain efficiency, achieving a gradient encoding scheme that is complementary to the spatial encoding provided by the receiver coils. This approach leads to "*O*-space" imaging, wherein the gradient shapes are tailored to an existing surface coil array, making more efficient use of the spatial information contained in the coil profiles. In its simplest form, for each acquired echo the Z2 spherical harmonic is used to project the object onto sets of concentric rings, while the X and Y gradients are used to offset this projection within the imaging plane. The theory is presented, an algorithm is introduced for image reconstruction, and simulations reveal that *O*-space encoding achieves high encoding efficiency compared to sensitivity encoding (SENSE) radial k-space trajectories, and parallel imaging technique with localized gradients (PatLoc), suggesting that *O*-space imaging holds great potential for accelerated scanning. Magn Reson Med 64:447–456, 2010. ©2010 Wiley-Liss, Inc.

Key words: nonlinear gradient encoding; O-space; parallel imaging; dynamic shimming; projection imaging

Parallel imaging methods exploit the spatial encoding provided by independent radio frequency (RF) coil profiles to perform image reconstruction from undersampled *k*-space data (1). Aliasing artifacts are removed using the spatial localization of the coil profiles to fill in missing phase-encode lines either in the image domain, as in sensitivity encoding (SENSE) (2), or in *k*-space, as in generalized autocalibrating partially parallel acquisitions (GRAPPA) (3). Parallel imaging performance is evaluated based on the geometry factor, or g-factor, which maps the amount of noise amplification that occurs in each voxel as a result of ill conditioning of the reconstruction problem due to linear dependence of the coil profiles (2,4). Extensive effort has been invested in optimizing coil profile orthogonality for a given region of interest (ROI) (5) and in exploring parallel imaging with undersampled non-Cartesian *k*-space trajectories (6). We propose to approach this problem in reverse: For the case of circumferentially distributed surface coils, we hypothesize that a radially symmetric gradient shape is a better complement to the coil array than a linearly varying gradient, thereby reducing the amount of data that must be acquired for imaging at a given resolution.

Gradient fields and radiofrequency coil profiles are based on fundamentally different physics and do not interfere with one another. They can therefore be freely combined to form encoding functions that are optimized for parallel imaging (7). Because linear gradient fields are described by plane wave encoding functions, which form the kernel of the Fourier transform integral, linear gradients permit fast and straightforward image reconstruction via the Fast Fourier Transform (FFT) once *k*-space is fully populated. However, linear gradients are not generally shaped so as to take maximum advantage of the spatial encoding inherent in surface coil profiles. Because of this, large numbers of independent coils are typically required to achieve low g-factors at high acceleration factors (8). At very high acceleration factors such as $R = 6$ or $R = 4 \times 4$, moving from 32 to 96 coils substantially lowers the g-factor, albeit at the expense of greatly increased hardware cost and complexity (9). However, at more practical reduction factors such as $R = 3$, $R = 4$, or even $R = 3 \times 3$, moving from 12 to 32 coils provides much more g-factor reduction than moving from 32 to 96 coils (9). As coil elements grow smaller and more numerous, mutual coupling is compounded and the ratio of unloaded-to-loaded quality factor generally decreases. Moreover, while large arrays do offer signal-to-noise ratio (SNR) improvements over volume coils, as the array size grows these gains are relegated to an ever-thinner band at periphery of the sample (10).

An alternative way to improve parallel imaging performance is to image at ultrahigh field strengths such as 7 T, where wave effects within the body dielectric cause a focusing of coil profiles, improving spatial localization and the ultimate achievable g-factor for a given acceleration factor (11). However, human imaging at 7 T is not yet widely available, especially in clinical settings, and presently entails technical complexities arising from magnet design, RF transmit field inhomogeneity, RF specific absorption rate, and other challenges (12).

Recently, nonbijective curvilinear gradients have been proposed to achieve faster gradient switching as well as spatially varying resolution tailored to object features of

[1]Department of Biomedical Engineering, Yale University, New Haven, CT.
[2]Department of Diagnostic Radiology, Yale University, New Haven, CT.
[3]Department of Radiology, Biomedical Engineering, and Neurosurgery, Yale University, New Haven, CT.

Grant sponsor: NIH; Grant number: 5T90DK070068-05.

*Correspondence to: Jason P. Stockmann, M.S., Yale MRRC, The Anlyan Center, 300 Cedar Street, P.O. Box 208043, New Haven, CT 06520.
E-mail: jason.stockmann@yale.edu

Received 16 September 2009; revised 13 January 2010; accepted 8 February 2010.
DOI 10.1002/mrm.22425
Published online in Wiley InterScience (www.interscience.wiley.com).

© 2010 Wiley-Liss, Inc.

interest (13,14). Known as "parallel imaging technique with localized gradients," or PatLoc, the method uses multipolar encoding fields based on the real and imaginary parts of the conformal mapping

$$f(z) = z^L = (x + iy)^L = u(x, y) + iv(x, y). \quad [1]$$

Because this mapping preserves the local angle between the isocontours of the inputs x and y, the vector gradients of fields u and v are everywhere orthogonal ($\nabla u \cdot \nabla v = 0$), permitting use of the two fields as frequency and phase-encoding gradients. Since z^L is analytic and satisfies Laplace's equation for all L, the shapes u and v are physically realizable. The resulting spherical harmonic fields of order L vary in polarity with angular position and grow as r^n, where r is the distance from the center.

For each coil, $N/(R_{pe}L)$ k-space lines are acquired, where R_{pe} is the k-space undersampling factor, for a net acceleration factor of $R = R_{pe}L$ as compared with a fully sampled conventional acquisition. The k-space data are Fourier transformed to yield L distorted and possibly aliased images in encoding space. Using a SENSE-like reconstruction, the spatial information provided by the surface coil profiles is used to map each point in the encoding space onto R_{pe} voxels in each of the L bijective regions in image space. The reduced B-field excursion over the bore of the scanner may permit faster gradient switching times for the same dB/dt as compared with linear gradients, potentially allowing for faster imaging without violating safety limits for peripheral nerve stimulation. However, the relatively flat frequency isocontours at the center of the field of view (FOV) cause pronounced blurring in this region.

In the O-space approach, parallel imaging performance is optimized using linear combinations of multiple spherical harmonics to form gradient shapes tailored to the spatial information contained in the coil profiles (15). In principle, different gradient shapes can be chosen for each successive echo to obtain suitable projections of the object. In the most general case, an array of surface coil profiles is selected and its spatial encoding properties are assessed. A nonlinear gradient encoding scheme is then designed so as to maximally complement the coils. In a typical circumferential coil array, the profiles vary smoothly throughout the FOV, with the area of peak sensitivity localized to the angular region subtended by each coil. A circumferential array therefore provides more encoding in the angular direction than in the radial direction, a fact that has not been exploited by past encoding schemes based on linear gradients alone.

For this study, we use a combination of the Z2 spherical harmonic and the X and Y gradients to image the axial plane. This choice of gradients is motivated by two factors: (1) the ability of the Z2 gradient to provide excellent spatial encoding along the radial direction, where circumferential coil arrays provide the least encoding; and (2) the ready availability of coil designs for producing the Z2 spherical harmonic (16). In this approach, conventional phase encoding is discarded and replaced by projection acquisitions with the center of the Z2 function shifted off center using the X and Y gradients. With each acquired echo, the object is projected onto a set of frequency isocontour rings that are concentric about a different center placement (CP) in the FOV, suggesting the term "O-Space imaging." By shifting the Z2 quadratic shape off center, it is ensured that there are enough overlapping isocontours from different projections at the center of the FOV to resolve features in this region.

The Fourier transform of an echo obtained in the presence of a radially symmetric gradient yields a projection of the object onto a set of concentric rings. With radial localization provided by the gradients, the surface coils are ideally positioned to provide spatial localization in the angular direction. Furthermore, as will be shown in the Results section, since the readout gradient provides spatial encoding in two dimensions, rather than just one as in Cartesian trajectories, additional encoding is provided by increasing the gradient strength and sampling the echo more densely, with essentially no impact on the imaging time. In Cartesian parallel imaging, densely sampling the echo increases resolution in the readout direction but does not reduce the amount of aliasing in the phase-encode direction.

THEORY

The Z2 gradient is translated to the desired CP in the FOV using linear gradients and a static field (B0) offset to complete the square (Fig. 1). Following slice selection, the X, Y, and Z2 gradients are used to dephase and rephase the spins, as in conventional projection imaging. The signal equation for echo $s(t)$ is

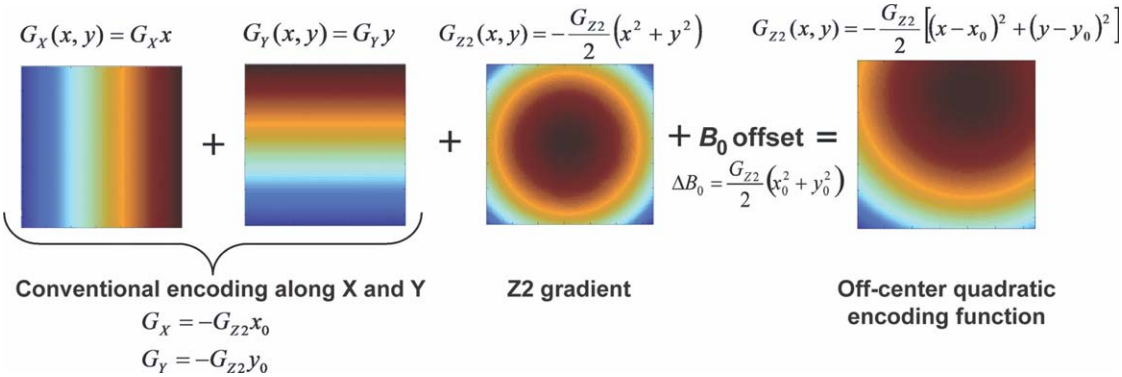


FIG. 1. Off-center parabolic frequency distributions are achieved by combining linear gradients and a constant field offset with the Z2 field to complete the square.

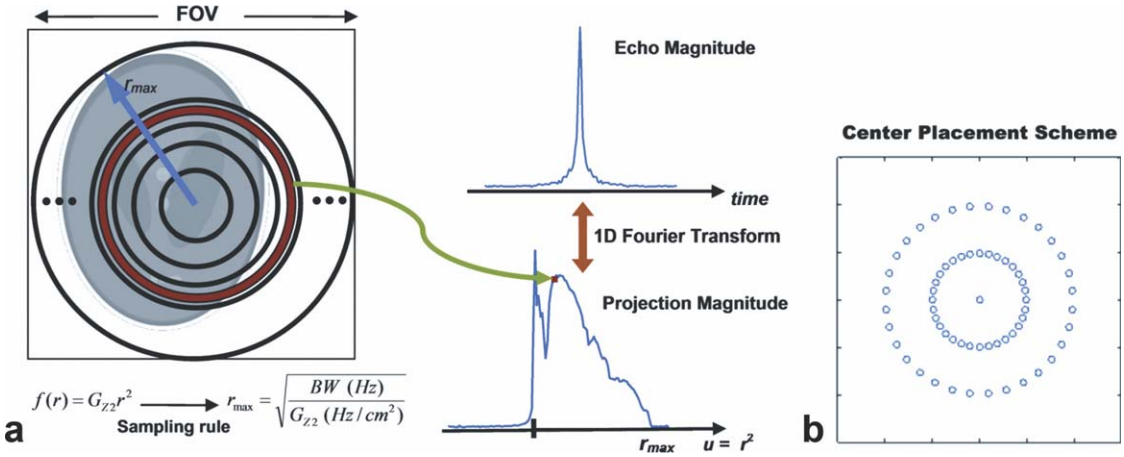


FIG. 2. **a**: Fourier transforming *O*-space echoes yields a projection of the object along a set of concentric rings. **b**: The selected 65 CPs correspond to successive echoes in an *O*-space acquisition. Datasets with 33 CPs and 17 CPs are obtained by skipping inner- and outer-ring CPs as appropriate.

$$s_{m,q}(t) = \iint \rho(x,y) C_q(x,y) \times \exp\left(-i2\pi G_{Z2} \frac{1}{2}\left((x-x_m)^2+(y-y_m)^2\right)t\right) dxdy = A_{m,q,t}\rho \quad (2)$$

where $\rho(x,y)$ is the object, $C_q(x,y)$ is the qth receive coil sensitivity, (x_m,y_m) specifies the mth CP, and G_{Z2} is the strength of the Z2 spherical harmonic in hertz/square centimeter. Gradient strengths G_X and G_Y are chosen such that $G_X = -G_{Z2}x_m$ and $G_Y = -G_{Z2}y_m$ in hertz/centimeter. Echoes formed using different CPs during successive pulse repetition times comprise a dataset from which the image is reconstructed. The number of CPs used to form an image is equivalent in terms of acquisition time to the number of phase encodes used in a conventional Cartesian sampled acquisition. In the discrete case, the integral kernel is represented as a projection matrix $A_{t,m,q}$ where rows describe time point, t, CP, m, and coil q, while the columns correspond to voxels in the object. The object ρ is vectorized and the echoes and encoding functions from multiple CPs and coils are stacked to produce a single matrix equation:

$$s = A\rho. \quad [3]$$

If radius r_m is defined relative to each CP, the integral may be recast in polar coordinates:

$$s_{m,q}(t) = \int\int \rho(r_m,\phi) C_q(r_m,\phi) \exp\left(-i2\pi G_{Z2} \frac{1}{2} r_m^2 t\right) r_m dr_m d\phi \quad [4]$$

With the choice of $u = \frac{1}{2}r_m^2$, the radial integral becomes a Fourier transform:

$$s_{m,q}(t) = \iint \rho(u,\phi) C_q(u,\phi) \exp(-i2\pi G_{Z2} u t) du d\varphi \quad [5]$$

The inverse Fourier transform of each echo now yields $P_{m,q}(u)$, the projection of the object along the isocontours encircling the mth CP. The projection specifies the amount of energy in the coil profile-weighted object that is smeared around ringlike regions which decrease in width as r_m increases (as in Fig. 2a).

Because the encoding function does not take the form of a Fourier integral kernel, the data do not reside in k-space. Consequently, image reconstruction cannot be achieved using k-space density compensation and regridding approaches similar to those employed in non-Cartesian imaging with linear gradients. Due to this fact, image reconstruction is performed by directly solving the matrix equation $s = A\rho$ using one of two methods: a spatial domain algorithm based on the projections and a frequency domain algorithm based on the echoes.

When projections are obtained using the discrete Fourier transform, each point in the projection $P_{m,q}[u]$ corresponds to the sum of the object intensity at all voxels lying within a band that can be approximated as the uth isofrequency ring. If N_s samples are acquired during readout, then there exist N_s isofrequency rings. The radius of the outermost ring is specified by

$$r_{max} = \sqrt{BW/G_{Z2}} \quad [6]$$

where BW is the sampling bandwidth. The sum over all voxels lying within a given ring is weighted by the qth surface coil profile at each point within the ring,

$$P_{m,q}[u] = \sum_{x,y \in ring\ u} C_q[x,y]\rho[x,y]. \quad [7]$$

When the object and coil profiles are represented in vector form, the set of all ring-domain equations may be vertically concatenated to form a single matrix equation accounting for all N_s rings, M CPs, and Q coils:

$$P[u] = [C^{\circ} W]\rho = E\rho \quad [8]$$

where $\circ$ denotes the element-wise product and W is a sparse matrix whose uth row weights each voxel according to its contribution to the uth ring of a given CP. The simplest version of W contains ones for each voxel lying

within the uth ring and zeroes elsewhere. For an $N \times N$ reconstruction, the encoding matrix E is of size [$N_s \times M \times Q$, $N \times N$]. Direct inversion of this matrix is challenging for practical matrix sizes, but the sparsity of the matrix can be exploited by a conjugate gradient-type algorithm known as "Sparse Equations and Least Squares" (LSQR) (17) that is available as a function call in MatLab (MathWorks, Natick, MA). LSQR was selected for its ability to quickly solve sparse, nonsquare, complex-valued matrix equations.

The spatial-domain reconstruction amounts to back-projecting points in each projection onto the corresponding rings in the image. The difficulty with this approach is in accounting for the spatially varying, complex-valued point spread function (PSF) of each applied gradient shape. Care must be taken in defining the boundary between rings. Radial Gibbs ringing of the PSF due to convolution with the Fourier transform of the acquisition window boxcar function must also be considered.

These obstacles can be surmounted by directly solving Eq. 3 in the frequency (echo) domain using the Kaczmarz iterative projection algorithm, also known as the algebraic reconstruction technique, a row-action method that has been applied to computed tomography and cryoelectron microscopy (18). This algorithm compares each echo time point with the inner product of the appropriate row of the projection matrix, denoted $a_{t,m,q}$, and the nth iterate of the image estimator. The difference between these scalars weights the amount of basis function $a_{t,m,q}$ that is added to the estimator going into the next iteration:

$$\hat{\rho}_{n+1} = \hat{\rho}_n + \lambda \frac{s_{t,m,q} - \langle a_{t,m,q}, \hat{\rho}_n \rangle}{\|a_{t,m,q}\|^2} a^*_{t,m,q} \qquad [9]$$

where * denotes complex conjugation. The algorithm typically converges in fewer than 10 iterations. The entire projection matrix is usually too large to fit in memory, precluding the use of LSQR as a MatLab call. But with the Kaczmarz approach, only one data point is treated at a time, permitting individual basis functions to be recomputed on the fly or loaded from the hard drive. For sufficiently small values of λ, underrelaxed Kaczmarz reconstructions have been shown to converge to the minimum-norm least-squares estimate for $\hat{\rho}$ (19), equivalent to that obtained using the pseudoinverse of A.

It should be noted that the shape of each "ring" can be approximated by Fourier transforming each $N_s \times N$ block of the encoding matrix along the time (row) dimension. These image-domain matrices can be assembled into an equation for the unknown image using the projection data (i.e., FFT of the echoes). This version of the encoding matrix can be sparsified by truncating all values falling below a certain threshold, leaving only the PSF in the vicinity of each ring. Using a sparse matrix that fits in memory, LSQR would present an attractive alternative to Kaczmarz for reconstructing the image, but we reserve this comparison for future work.

MATERIALS AND METHODS

Simulations were used to investigate O-space imaging in more detail. First, LSQR image-domain reconstructions at low resolution were used to quickly explore a variety of CP schemes to identify one that provides efficient O-space encoding. Second, once a CP scheme was chosen, Kaczmarz frequency-domain reconstructions at high resolution were used to compare O-space with SENSE, PatLoc, and radial reconstructions over a wide range of acceleration factors. Third, Kaczmarz reconstructions were used to investigate the degradation of O-space and SENSE reconstructions in the presence of increasing amounts of noise. Fourth, Kaczmarz simulations were used to explore the effect of increased ring density on the resolution of O-space images.

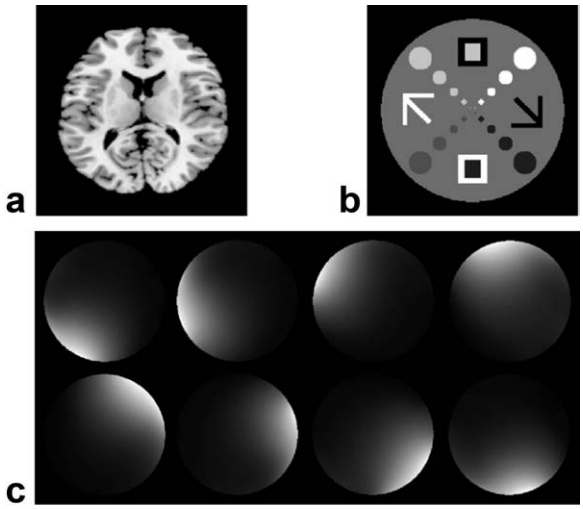


FIG. 3. **a**: Brain phantom. **b**: Numerical phantom. **c**: Measured 256 × 256 surface coil profiles from the eight-channel array for use in simulations.

Two phantoms were used for each Kaczmarz simulation: an axial brain image (Fig. 3a) obtained using a conventional acquisition and a numerical phantom (Fig. 3b) designed to illustrate the spatially varying resolution and contrast properties of O-space encoding gradients. The numerical phantom incorporates small lesionlike features at four contrast levels, as well as sharp edges in the X and Y directions.

In the LSQR simulations, 128 × 128 reconstructions from 128-point echoes were used to determine a highly efficient CP scheme within the FOV for datasets composed of 32 and 16 echoes (20). By analogy to Cartesian parallel imaging, this corresponds to 4-fold and 8-fold undersampling, respectively. A variety of coil geometries were also considered, ranging from eight to 32 circumferentially distributed loop coils, for which B-fields can be approximated in the magnetostatic limit using the exact analytical field expression for circular loops (21). For simplicity and computational efficiency, a ring approximation to the true PSF was used in which each voxel whose center lies between two frequency isocontours was blurred evenly over all voxels enclosed between the two contours.

Once a highly efficient CP scheme was chosen, the Kaczmarz algorithm was used to perform reconstructions by directly solving the frequency-domain matrix representation of the signal equation for simulated 512-point

echoes. *O*-space 256 × 256 reconstructions were compared to time-equivalent SENSE, PatLoc, and radial reconstructions for $R = \{4, 8, 16\}$. Since the scope of this study is limited to two-dimensional imaging, SENSE acceleration was only performed along one phase encode direction. PatLoc reconstructions were performed using $L=2$ multipolar fields with undersampling of the phase-encode *k*-space by factors of 2, 4, and 8, yielding net acceleration factors of $R = \{4, 8, 16\}$.

Previous studies have shown high-quality parallel reconstructions from undersampled multicoil radial *k*-space data (22). If the Z2 gradient is turned off during an *O*-space acquisition, what remains in the case of a circular arrangement of CPs closely resembles a radial acquisition. In this vein, a comparison between *O*-space and undersampled radial reconstructions is useful for isolating the effect of the extra encoding provided by the addition of the Z2 gradient. For radial reconstructions, the Nyquist criterion requires $N\pi/2$ spokes for an image of size *N*. However, for ease of comparison against the SENSE, PatLoc, and *O*-space images, radial reconstructions using N/R spokes were considered to be "*R* undersampled," neglecting the extra factor of $\pi/2$ in the undersampling factor. Radial reconstructions were performed using $N\sqrt{2}$ readout points per spoke, consistent with the Nyquist criterion for a fully sampled radial dataset. For further ease of comparison, the Kaczmarz algorithm was used to reconstruct the radial images based on the full encoding matrix.

Gaussian noise was added to each point of the simulated echoes. The noise standard deviation was scaled relative to the mean intensity in the phantom and then further scaled by the phantom dimension *N* to account for two-dimensional Fourier transformation into the frequency domain. Noise correlations between the coil channels were neglected for the purposes of this study and will be treated in future work. It is expected that these correlations will similarly impact both conventional Cartesian SENSE reconstruction and the proposed *O*-space approach.

For the $R = 4$ case, *O*-space and SENSE reconstructions were compared in the presence of varying amounts of noise. Noise amplification in the SENSE reconstructions was mitigated using Tikhonov regularization via the truncated singular value decomposition (SVD) of the aliasing matrix (23).

To explore the effects of ring density on resolution, the readout window was held constant while gradient strength and the number of readout points (N_s) were incrementally increased. Extra channel noise was injected into the echoes to model the increased sampling bandwidth. Care was taken not to exceed practical gradient strengths for a Z2 coil design.

For proof that an image can be obtained with an *O*-space acquisition scheme, experimental data were collected on a 4.7-T Bruker animal magnet (Billerica, MA) operating at 4-T (total bore diameter = 310 mm) with a Bruker Avance console. The system is equipped with dynamic shimming updating on all first- and second-order gradients that can be triggered from within a pulse sequence (24).

Because the dynamic shimming updating system and the Z2 shim coil were designed for multivoxel spectroscopy (25) rather than spatial encoding, the imaging sequence had to be carefully tailored around the constraints imposed by the Z2 coil's limited strength (600 Hz/cm^2), slow rise time, and lack of shielding. The eddy current effects of the Z2 gradient were measured by switching the Z2 coil on, waiting 150 ms, switching the coil off, and acquiring one-dimensional projections of a thin tube phantom oriented along the z-axis at various delays after the Z2 falling edge. A second-order fit to the resulting phase profiles along the z-direction provided a measure of the Z0 and Z2 eddy current fields as a function of time. Based on these measurements, a 25-ms pad time was inserted into the *O*-space imaging sequence between the rising edge of the readout gradient and the acquisition window in order to allow for transient Z0 and Z2 fields to fall to less than 5 Hz and 2 Hz/cm^2, respectively.

In order to avoid radial aliasing in *O*-space, the sampling bandwidth and Z2-gradient strength G_{Z2} were chosen so that the outermost frequency ring did not fall within the object for a particular CP. In practice, even with the Z2 coil set to full strength over a 50-ms echo, most of the sampled rings lay outside the phantom, leading to suboptimal encoding, specific to this gradient set but not to the approach.

Because of the long echo length, off-resonance effects were deleterious to the phase-sensitive Kaczmarz reconstructions, even in a carefully shimmed phantom. This obstacle was overcome by forming a composite echo for each CP, using $N_s = 256$ separate acquisitions, each employing a variable-strength dephasing lobe to shift the gradient echo away from the spin echo by an integer number of dwell times. Each acquired echo thus provides one phase-corrected data point at the spin echo time. It is expected that this phase correction would not be necessary with a stronger Z2 gradient that enabled shorter echo lengths.

The amplitude of scanner B0 field drift was monitored periodically throughout the course of a scan by turning off all gradients and recording an free induction decay (FID). Off-resonance phase evolution was then removed from each acquired echo by subtracting out the phase of the FID on a pointwise basis.

Gradient Calibration

Accurate knowledge of the applied gradient strengths during *O*-space image reconstruction ensures that rings from different CPs overlap at the appropriate voxels. Calibration of the Z2 gradient was performed at nine points over the entire range of available gradient strengths (±600 Hz/cm^2 for Z2). For each Z2 strength, gradient echo images were acquired over 16 slices in a 4-cm FOV with Δ TE (echo time) = {0, 0.18, 1.0, 3.0} ms. At each voxel, the phase was plotted versus ΔTE and the frequency was found by calculating the slope of the line. The first two points in the line were used to unwrap the phase of the last two points, whose purpose was to reduce the noise in the slope estimate (26). FMAP software (27) was used for ROI selection, phase unwrapping, and calculation of the spherical harmonic components (X, Y, and Z2) in each frequency map.

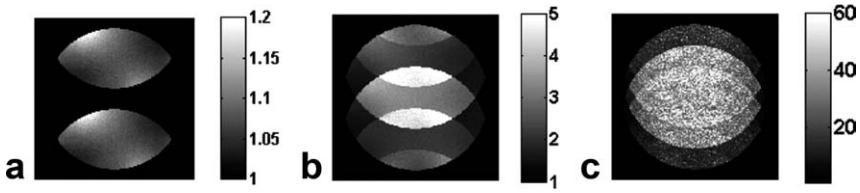


FIG. 4. Maps of the g-factor for acquired coil profiles from the eight-channel array. **a**: $R = 2$, $g_{mean} = 1.05$, $g_{max} = 1.22$. **b**: $R = 4$, $g_{mean} = 2.6$, $g_{max} = 6.54$. **c**: $R = 8$, $g_{mean} = 30.3$, $g_{max} = 661$.

Unfortunately, since only one receiver channel was available on the system equipped with dynamic shim updating, multicoil *O*-space acquisitions could not be performed. Coil profiles for use in the Kaczmarz simulations were obtained from an eight-channel Invivo knee coil array (Orlando, FL) on a Siemens 3-T Tim Trio system (Erlangen, Germany).

RESULTS

The CP scheme yielding the minimum mean squared error reconstruction in LSQR simulations is shown in Fig. 2b. The phantoms and coil profiles (12-cm FOV) used in the high-resolution Kaczmarz simulations are shown in Fig. 3. For reference, the g-factor was computed (2) for SENSE for several acceleration factors (Fig. 4).

In the high-resolution $R = 4$ reconstructions with 5% noise, *O*-space images displayed comparable resolution and slightly lower noise levels as compared with SENSE images (Fig. 5). At $R = 8$, however, the SENSE reconstruction with eight coils becomes ill conditioned and either entirely overwhelmed by noise (as shown here) or plagued by severe residual artifacts, depending on the Tikhonov regularization parameter selected. By contrast, the *O*-space reconstruction at $R = 8$ shows a mild increase in noise and loss of resolution. At $R = 16$, an acceleration factor for which SENSE reconstructions are impossible with only eight coils, *O*-space images suffer some blurring of small features but retain impressive resolution and noise levels for images based on only 16 projections.

PatLoc reconstructions at $R = 4$ show low levels of noise amplification, indicating that the encircling surface coils are complementary to multipolar PatLoc encoding fields; that is to say, the coils are well positioned to

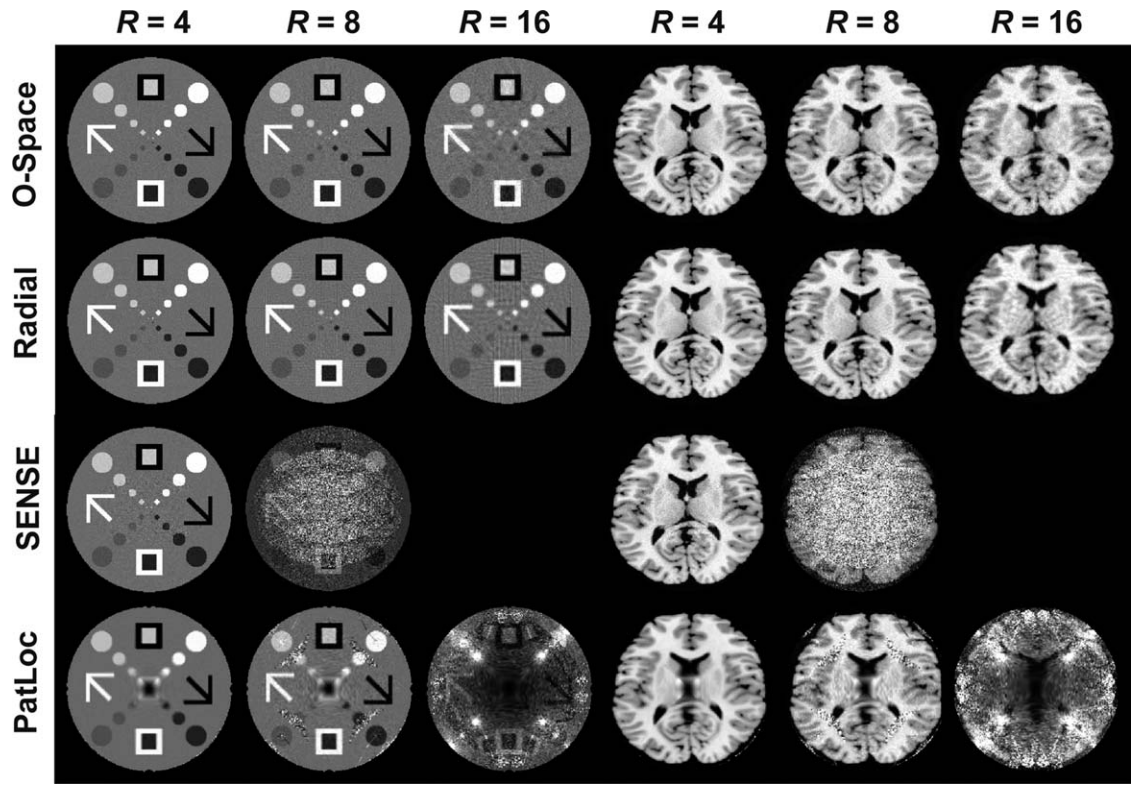


FIG. 5. Comparison of *O*-space, radial, SENSE, and PatLoc 256 × 256 reconstructions as a function of acceleration factor for an eight-coil array with moderate noise (5% of mean phantom intensity). As *R* increases beyond 4, the SENSE and PatLoc reconstructions rapidly deteriorate. By contrast, *O*-space performance degrades gradually, displaying only moderate noise amplification and blurring of small features. *O*-space reconstructions show promise even when *R* exceeds the number of coils, a scenario not possible with SENSE. Radial reconstructions perform more comparably to *O*-space reconstructions, but at $R = 16$, the radial images show streaking artifacts (see numerical phantom) and loss of feature discrimination (particularly around the ventricles of the brain phantom).

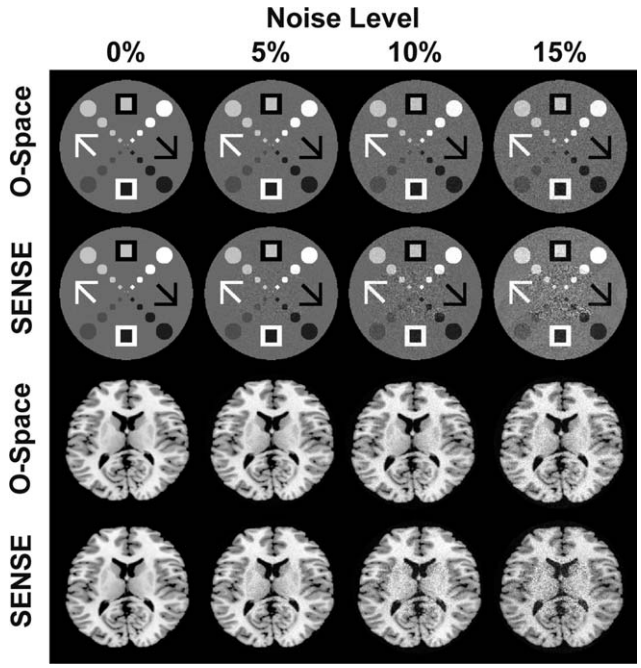


FIG. 6. Noise levels for eight-coil *O*-space and SENSE reconstructions at $R = 4$. While SENSE is highly sensitive to noise and requires regularization to prevent noise amplification from dominating the image, *O*-space reconstructions degrade gracefully even when the data are highly noisy. In addition, *O*-space noise is distributed more evenly throughout the FOV, while SENSE noise is concentrated in areas of high g-factor.

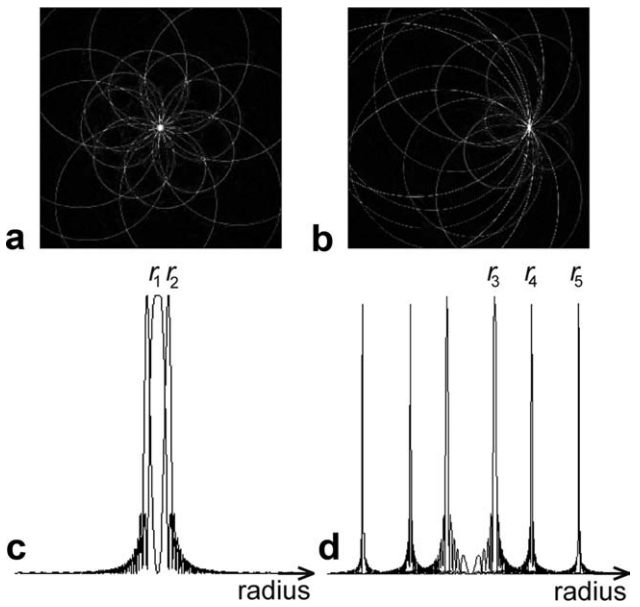


FIG. 7. Spatially varying *O*-space PSF of the 16-CP scheme used in simulations for a point source of unit intensity located at voxel $(x, y) = (0,0)$ (**a**) and $(x, y) = (75,0)$ (**b**) within a 256 $\times$ 256 FOV. The scale is compressed 10-fold to bring out low-level ring features. For projections formed using the Z2-gradient alone (**c,d**), horizontal profiles through the ring projections illustrate the poor radial resolution of the two centermost rings at r_1 and r_2 (**c**) in contrast to the fine resolution of rings at the larger radii r_3, r_4, and r_5 (**d**).

localize signal from each acquired point in encoding space back onto the source voxels in the two bijective regions of image space. As the net acceleration factor approaches the number of coils, however, noise amplification grows severe in parts of each bijective region. As expected, resolution degrades near the center of the FOV as the spatial derivative of the encoding fields approaches zero. In this region, the coil profiles do not provide adequate localization to make up for the lost encoding from linear gradients.

O-space and radial reconstructions performed comparably at low acceleration factors, each displaying excellent resolution at $R = 4$. At $R = 8$, the streaking artifacts in radial images become more pronounced, while the *O*-space artifacts remain incoherent enough to avoid clear manifestation in the image. The *O*-space images do exhibit slightly higher noise levels, in part because of the higher readout bandwidth of the simulated 512-point *O*-space echoes. At $R = 16$, *O*-space demonstrates a clear advantage over radial, with the *O*-space brain image preserving more detail in the areas around the venctricles.

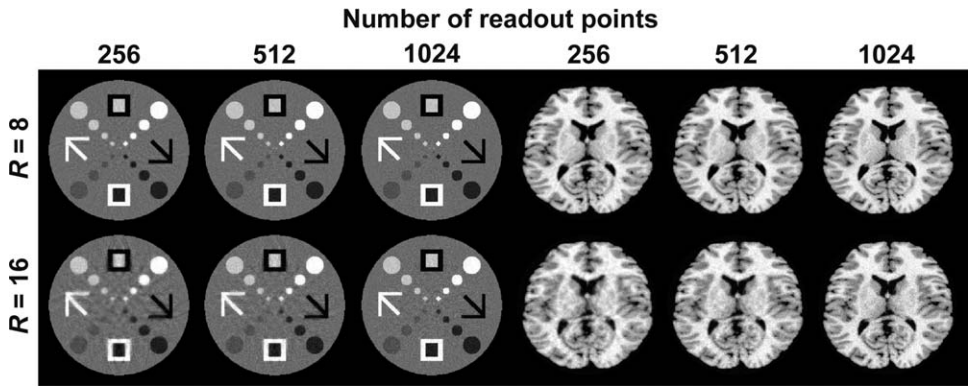


FIG. 8. Time-equivalent $R = 8$ and $R = 16$ *O*-space 256 $\times$ 256 phantom reconstructions based on 256 rings, 512 rings, and 1024 rings per echo, along with corresponding brain simulations. Resolution improves as ring density is increased within the object. Uncorrelated noise with standard deviation equal to 5% of the mean phantom intensity was added during echo simulation. The noise is then scaled by $\sqrt{2}$ and $\sqrt{4}$ in the 256- and 512-point reconstructions, respectively, to reflect the increased sampling bandwidth.

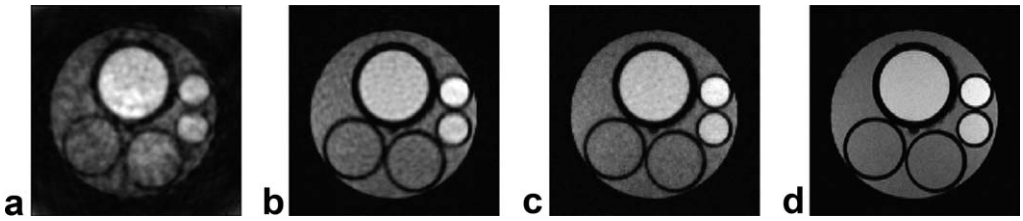


FIG. 9. *O*-space reconstruction (**a**) using acquired data from a volume coil with 65 CPs (128 × 128 voxels, FOV = 3 cm). Cartesian spin echo reference image (**d**) acquired at the same echo time (210 ms). *O*-space simulations based on the reference image are shown for the actual (**b**) and optimal (**c**) gradient strengths.

When the acceleration factor is held constant at $R = 4$ and the noise level is varied (Fig. 6), the noise in *O*-space reconstructions is both lower and more spatially uniform than the noise in SENSE reconstructions, which concentrates in regions of high g-factor. In *O*-space imaging, each voxel is smeared out along rings according to the spatially varying PSF of each CP, preventing noise from concentrating in any one region of the image.

Approximations to the PSF were obtained from the matrix product $A^H A$, where A^H denotes the conjugate transpose of the encoding matrix. Each row of $A^H A$ is the vectorized PSF for a particular voxel in the FOV. To isolate the effects of the gradient encoding alone, a single coil with uniform sensitivity was used. Representative PSFs for the 16-CP encoding scheme are shown (Fig. 7a,b); for each CP, the source voxel blurs along a ring that has the CP at its origin. The source is localized to the point where all 16 rings overlap, with additional localization provided when a surface coil array is used.

To illustrate the encoding provided by the Z2 gradient alone, the encoding matrix for the Z2 gradient shape was Fourier transformed along the temporal dimension (row-wise), yielding the ringlike shapes that correspond to each point in a Z2 projection. Magnitude plots of a horizontal profile through the center of the FOV (Fig. 7c,d) illustrate the radial variation in resolution and the effects of echo truncation. Since the spatial derivative of the Z2 field shape is zero at the center of the FOV, nearly all gradient encoding in this region comes from the application of the X and Y gradients to shift the rings off center. Truncation of an echo with a window of duration τ results in convolution of the rings with $\mathrm{sinc}(2u/\tau)$ in u-space, corresponding to $\mathrm{sinc}(2r^2/\tau)$ in the image domain. This leads to widening of the side lobes as r approaches zero.

As expected, increased ring density within the phantom contributes to significant improvements in resolution. *O*-space reconstructions with only 256 rings show substantial blurring and background nonuniformity at $R = 16$ (Fig. 8), suggesting that setting N_s equal to N does not provide enough rings for highly accelerated acquisitions. But as the number of rings is increased to 512 and 1024, resolution improves noticeably in the $R = 8$ case and substantially in the $R = 16$ case. This stands in contrast to Cartesian acquisitions, where increasing the readout gradient strength provides no reduction in aliasing artifacts along the undersampled direction(s). In principle, the achievable *O*-space ring density in the sample is limited only by (1) the diminishing SNR provided by very thin rings and (2) safety regulations on gradient switching rates. It should be emphasized that increasing the number of samples in the readout and sampling faster (higher bandwidth) does not change the overall imaging time, and thus the imaging time along a row in Fig. 8 is constant.

Volume-coil datasets acquired with the dynamic shimming Z2 gradient used 64 CPs distributed around the center of the FOV, a 65th echo using just the Z2 gradient, and a series of FIDs with no applied gradients to monitor scanner frequency drift. The reconstruction in Fig. 9a shows that *O*-Space reconstructions are possible even when suboptimal gradients are used. It also demonstrates two principal types of artifacts: those arising from systematic errors in the gradient calibrations and those caused by the limited available Z2-gradient strength. Comparison of a simulated reconstruction using the actual acquisition parameters (Fig. 9b) with a simulation using ideal, "Nyquist-sampled" readouts (Fig. 9c) shows that most of the artifacts in a single-coil $R = 1.97$ acquisition can be eliminated if an adequately strong Z2 gradient is used.

Implementing *O*-space imaging on a clinical scanner would entail the construction of a shielded gradient insert capable of generating a Z2 gradient with high amplitude and fast rise time. This would also require two gradient amplifiers, one for driving the Z2 term and another to compensate for any shifts in B0 as a function of the Z2 gradient. Alternatively, and preferably, such a gradient would be built into the manufacturer's standard body coil, thereby increasing the range of acquisition strategies possible with parallel imaging sequences. It should also be noted that the *O*-space acquisitions strategy can be adapted to almost any pulse sequence that has a dephase gradient followed by a readout gradient, where the dephase/rephase gradients now use different combinations of X, Y, and Z2 for each CP.

CONCLUSION

Preliminary single channel reconstructions provide a proof of concept for *O*-space imaging while indicating that the method could be substantially improved through the use of a stronger Z2-gradient field and more accurate gradient calibration. Simulations show that *O*-space imaging outperforms Cartesian SENSE and PatLoc when the effective acceleration factor approaches, equals, or exceeds the number of coils used. Similarly, at very high acceleration factors, comparisons of *O*-space and radial

reconstructions demonstrate that useful encoding is in fact provided through the addition of the Z2 gradient to a radial-like projection imaging sequence. Although the gradient isocontours from each pair of CPs are not orthogonal for all voxels in the FOV, the extra information extracted from the surface coil profiles appears to more than compensate for the linear dependence between the different gradient shapes. This suggests that evaluations of parallel imaging performance should be based on the orthogonality of the hybrid encoding functions formed using different combinations of complementary gradient shapes and coil profiles and not merely on the independence of the coil profiles from one another along each phase-encode direction.

Investigators have begun searching for ways to obtain and evaluate the optimal gradient shapes to complement a particular surface coil array (28). One approach uses the singular value decomposition of coil profiles to find the orthogonal modes of the coil profiles and then specifies pairs of frequency/phase encoding PatLoc gradients that approximate these modes (29). Because they satisfy Laplace's equation, spherical harmonics form one appealing basis set with which to approximate desired gradient shapes. In principle, linear combinations of spherical harmonics may be used to create linearly independent projections of the object at each echo. As the object is projected onto each of these basis functions, successive echoes capture object features that were not resolved in the preceding echoes. Orthogonality between all pairs of spherical harmonics exists only over a spherical volume. This suggests that a suitable combination of first-order and higher-order spherical harmonics, an extension of the approach used in this paper, might be suitable for three-dimensional imaging.

Encoding efficiency depends on the combination of the coil and gradient encoding functions. In principle, there is more freedom to tailor the gradient shape to the coil sensitivity functions than vice versa. The radiofrequency nearfields produced by surface coils are smoothly varying functions that track the coil aperture and shape to some extent but cannot be significantly narrowed or focused without moving to a higher B0 strength. With the use of higher-order spherical harmonics as gradient encoding functions, there is great promise in choosing optimal gradient shapes for the ROI and the coil array in use. This work demonstrates that, in principle, highly accelerated, multicoil, nonlinear *O*-space projections can produce images that are superior to time-equivalent SENSE and radial reconstructions. Preliminary data obtained from a Z2 dynamic shim coil show that *O*-space reconstructions are sensitive to uncertainty in the gradient strength and B0 offset but that this obstacle can be overcome through careful calibration. Future work will investigate the performance of multicoil acquired *O*-space data using a stronger Z2-gradient insert, methods for speeding image reconstruction by exploiting patterns in the encoding matrix, and metrics for choosing optimal physically realizable gradient shapes for a given surface coil array.

ACKNOWLEDGMENTS

The authors thank Hemant Tagare, Christoph Juchem, Robin de Graaf, Peter Brown, Terry Nixon, Doug Rothman, Laura Sacolick, and Richard Carson, each of whom provided valuable insights into the problem of nonlinear gradient encoding or indispensable expertise during our experiments.

REFERENCES

1. Sodickson DK, Manning WJ. Simultaneous acquisition of spatial harmonics (SMASH): fast imaging with radiofrequency coil arrays. Magn Reson Med 1997;38:591–603.
2. Pruessmann KP, Weiger M, Scheidegger MB, Boesiger P. SENSE: sensitivity encoding for fast MRI. Magn Reson Med 1999;42:952–962.
3. Griswold MA, Jakob PM, Heidemann RM, Nittka M, Jellus V, Wang J, Kiefer B, Haase A. Generalized autocalibrating partially parallel acquisitions (GRAPPA). Magn Reson Med 2002;47:1202–1210.
4. Breuer FA, Kannengiesser SA, Blaimer M, Seiberlich N, Jakob PM, Griswold MA. General formulation for quantitative g-factor calculation in GRAPPA reconstructions. Magn Reson Med 2009;62:739–746.
5. Ohliger MA, Sodickson DK. An introduction to coil array design for parallel MRI. NMR Biomed 2006;19:300–315.
6. Pruessmann KP, Weiger M, Bornert P, Boesiger P. Advances in sensitivity encoding with arbitrary k-space trajectories. Magn Reson Med 2001;46:638–651.
7. Pruessmann K. Encoding and reconstruction in parallel MRI. NMR Biomed 2006;19:288–299.
8. Wiggins GC, Triantafyllou C, Potthast A, Reykowski A, Nittka M, Wald LL. 32-Channel 3 tesla receive-only phased array head coil with soccer-ball element geometry. Magn Reson Med 2006;56:216–223.
9. Wiggins GC, Polimeni JR, Potthast A, Schmitt M, Alagappan V, Wald LL. 96-Channel receive-only head coil for 3 tesla: design optimization and evaluation. Magn Reson Med 2009;62:754–762.
10. King SB, Varosi SM, Duensing GR. Eigenmode analysis for understanding phased array coils and their limits. Con Magn Reson B 2006;29B:42–49.
11. Wiesinger F, Boesinger P, Pruessmann KP. Electrodynamics and ultimate SNR in parallel MR imaging. Magn Reson Med 2004;52:376–390.
12. Vaughan JT, Snyder CJ, DelaBarre LJ, Bolan PJ, Tian J, Bolinger L, Adriany G, Andersen P, Strupp J, Ugurbil K. Whole-body imaging at 7T: preliminary results. Magn Reson Med 2009;61:244–248.
13. Hennig J, Welz AM, Schultz G, Korvink J, Liu Z, Speck O, Zaitsev M. Parallel imaging in non-bijective, curvilinear magnetic field gradients: a concept study. MAGMA 2008;21:5–14.
14. Welz AM, Zaitsev M, Lehr H, Schultz G, Liu Z, Jia F, Post H, Korvink J, Hennig J. Initial realization of a multichannel, nonlinear PatLoc gradient coil. In: Proceedings of the ISMRM 16th Annual Meeting, Toronto, Ontario, 2008. p 1163.
15. Stockmann JP, Ciris PA, Constable RT. Efficient "*O*-space" parallel imaging using non-linear encoding fields with no phase encoding. In: Proceedings of the ISMRM 17th Annual Meeting, Honolulu, HI, 2009. p 761.
16. Romeo F, Hoult DI. Magnetic field mapping: analysis and correcting coil design. Magn Reson Med 1984;1:44–65.
17. Paige CC, Saunders MA. LSQR: an algorithm for sparse linear equations and sparse least squares. ACM Trans Math Software 1982;8:43–71.
18. Herman GT, Lent A. Iterative reconstruction algorithms. Comput Biol Med 1976;6:273–294.
19. Censor Y, Eggermont PPB, Gordon D. Strong underrelaxation in Kaczmarz's method for inconsistent systems. Numer Math 1983;41:83–92.
20. Ciris PA, Stockmann JP, Constable RT. O-space imaging: tailoring encoding gradients to coil profiles for highly accelerated imaging. In: Proceedings of the ISMRM 17th Annual Meeting, Honolulu, HI, 2009. p 4556.
21. Smythe WR. Static and dynamic electricity. New York: McGraw-Hill; 1968. 608 p.
22. Block KT, Uecker M, Frahm J. Undersampled radial MRI with multiple coils: iterative image reconstruction using a total variation constraint. Magn Reson Med 2007;57:1086–1098.
23. Lin F, Kwong KK, Belliveau JW, Wald LL. Parallel imaging reconstruction using automatic regularization. Magn Reson Med 2004;51:559–567.

24. De Graaf RA, Brown P, McIntyre S, Rothman DL, Nixon T. Dynamic shim updating (DSU) for multislice signal acquisition. Magn Reson Med 2003;49:409–416.
25. Koch KM, Sacolick LI, Nixon TW, McIntyre S, Rothman DL, de Graaf RA. Dynamically shimmed multivoxel ^{1}H magnetic resonance spectroscopy and multislice magnetic resonance spectroscopic imaging of the human brain. Magn Reson Med 2007;57:587–591.
26. De Graaf RA. In vivo NMR spectroscopy: principles and techniques. Chichester, UK: John Wiley & Sons; 2008.
27. Juchem C. FMAP field mapping software version 9 release 8, Yale Univ. MRRC, Aug. 2008.
28. Tam LK, Stockmann JP, Ciris PA, Constable RT. Non-linear encoding gradient optimization for *O*-space imaging with a microstrip coil array. In: Proceedings of the ISMRM 17th Annual Meeting, Honolulu, HI, 2009. p 3072.
29. Lin F. Parallel imaging technique using localized gradients (PatLoc) reconstruction using orthogonal mode decomposition. In: Proceedings of the ISMRM 17th Annual Meeting, Honolulu, HI, 2009. p 4557.